Monthly Notices of the ROYAL ASTRONOMICAL SOCIETY

MNRAS **536,** 2421–2432 (2025) https://doi.org/10.1093/mnras/stae2720
Advance Access publication 2024 December 10

Little iLocater: paving the way for iLocater

Robert J. Harris ,[1★] Jonathan Crass ,[2,3] Marshall C. Johnson ,[2] Andrew J. Bechter ,[3]
Jennifer Power,[4] Ariadna Calcines Rosario ,[1] Justin R. Crepp ,[3] Eric B. Bechter ,[3] Brian L. Sands ,[5]
Derek Kopon , Steve Ertel ,[6,7] Santiago Barboza[8] and Andrea Bianco [9]

[1] *Centre for Advanced Instrumentation, Department of Physics, Durham University, South Road, Durham DH1 3LE, UK*
[2] *Department of Astronomy, The Ohio State University, 4055 McPherson Laboratory, 140 West 18th Avenue, Columbus, OH 43210, USA*
[3] *Department of Physics & Astronomy, University of Notre Dame, 225 Nieuwland Science Hall, Notre Dame, IN 46556, USA*
[4] *Large Binocular Telescope Observatory, The Univeristy of Arizona, 933 N. Cherry Ave, Tucson, AZ 85721-0065, USA*
[5] *Engineering & Design Core Facility, University of Notre Dame, 626 Flanner Hall, Notre Dame, IN 46556, USA*
[6] *Department of Astronomy and Steward Observatory, The University of Arizona, 933 North Cherry Ave, Tucson, AZ 85721, USA*
[7] *Large Binocular Telescope Observatory, The University of Arizona, 933 North Cherry Ave, Tucson, AZ 85721, USA*
[8] *Max-Planck-Institute for Astronomy, Königstuhl 17, D-69117 Heidelberg, Germany*
[9] *INAF – Osservatorio Astronomico di Brera, via E. Bianchi 46, I-23807 Merate (LC), Italy*

Accepted 2024 December 3. Received 2024 November 29; in original form 2024 August 1

ABSTRACT

Diffraction-limited radial-velocity instruments offer a pathway towards improved precision and stability, and the exploration of new parameter spaces at high spatial and spectral resolution. However, achieving the necessary performance requires careful instrument design and considerable on-sky testing. We describe the design and construction of 'Little iLocater' (Lili), a compact spectrograph that has been used to validate the performance of the front-end fibre-injection system of the iLocater spectrograph. We present the design, assembly, and performance using on-sky data obtained at the Large Binocular Telescope (LBT), including extraction of spectra from standard stars, testing of the atmospheric dispersion corrector to elevations of 40°, and spatially resolved spectra from close companion systems. These results show the front-end fibre-injection system is performing as expected and is indicative of iLocater's capabilities once installed at the LBT.

Key words: instrumentation: adaptive optics – instrumentation: spectrographs – techniques: high angular resolution.

1 INTRODUCTION

Spectrographs providing precise radial velocity measurements of stars are a key tool for the detection and characterization of exoplanets and the stars they orbit. Several next-generation instruments use adaptive optics (AO) for fibre injection (e.g. Gibson et al. 2019; Crass et al. 2021; Lovis et al. 2022; Mawet et al. 2022; Sliski et al. 2023; Vigan et al. 2024), allowing increased spatial resolution and spectral resolution, the elimination of spatial modal noise, a stable line spread function, reduction in on-sky background contamination, and a smaller spectrograph to be built, thus improving instrument stability and precision (Bland-Hawthorn & Horton 2006; Crepp 2014). However, building these instruments remains a challenge, as numerous error sources can combine to reduce measurement precision for the instrument overall (Bechter et al. 2018, 2019, 2020). Testing of critical components and observing modes is vital to the ultimate success of the spectrograph.

1.1 Fibre optics in astronomy

Fibre optics allow the efficient and flexible transport of light from one location to another and are integrated into many aspects of everyday life. Initially, fibre-fed instruments were designed to couple starlight from seeing-limited telescopes. In order to do this efficiently, the fibres were required to have cores of order 100 microns in diameter. While large mode field diameters offer high throughput, seeing-limited spectrographs on large telescopes require proportionally larger diffraction gratings to generate sufficient resolution (Bland-Hawthorn & Horton 2006; Spaleniak et al. 2013). This relationship is particularly problematic in the era of Extremely Large Telescopes (ELTs), where high-resolution seeing-limited spectrographs need to be the size of a small house.

1.2 Single-mode fibres and photonic lanterns

Single-mode fibres (SMFs) are fibres with cores of order 10 µm that only support a single mode (excluding polarization, which allows two modes to propagate). To couple efficiently into this mode, a near Gaussian beam is required, with a flat phase profile. Interferometric instruments were early adopters of SMFs, as having only one spatial mode means having to only compensate for one delay (effective index) between telescopes. This has allowed the development of fibre-fed instruments like the Fiber Linked Unit for Optical Recombination (FLUOR) (Scott et al. 2013) at the Center for High Angular Resolution Astronomy (CHARA) and the VLT INterferometer Commissioning Instrument (VINCI) (Kervella

---

★ E-mail: robert.j.harris@durham.ac.uk

Table 1. Parameters of the C-RED 2 detector as per specifications. Note, we only specify the parameters for low and high gain as these were the only modes used on-sky.

Parameter	Value
Pixels	640 × 512
Pixel pitch (µm)	15
Max frame rate (Hz)	400
Read noise (e-)	<30
Dark current (e-/p/s)	<600
Full well capacity (ke-)	1400 (low) 33 (high)

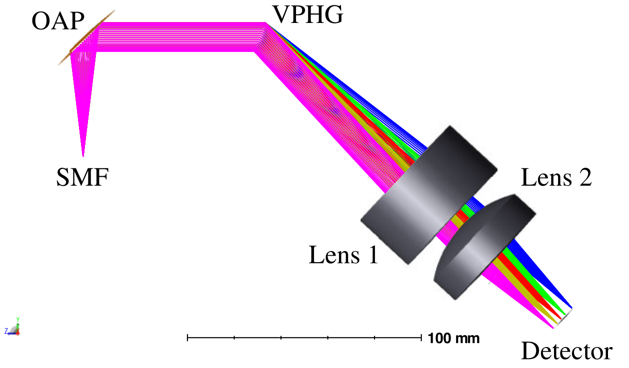

Figure 1. Shaded rendering of the optical design of the Lili spectrograph, with the light path coloured by wavelength. From left to right, the light from the SMF is collimated by an off-axis parabola (OAP), which feeds a VPH grating. Light is then refocused on to the detector by a TTL200-S8 and AC-508-080-C lens.

et al. 2003), the Precision Integrated-Optics Near-infrared Imaging ExpeRiment (PIONEER) (Le Bouquin et al. 2011) and GRAVITY (GRAVITY Collaboration 2017) at the Very Large Telescope (VLT).

The major drawback of using an SMF input is that unless the image remains diffraction-limited and stable, coupling efficiencies degrade significantly (Jovanovic et al. 2017). Thus, the use of SMF in spectroscopy was not considered an effective solution for years. Recently, two different avenues have emerged to make the use of SMF in spectroscopy viable.

The first approach benefits from the increased adoption of AO on large-aperture telescopes. AO restores the spatial resolving power of a telescope to the diffraction limit, instead of that set by the atmosphere. Background noise is reduced by 1–2 orders of magnitude when focusing light into a smaller region (Crepp 2014; Crass et al. 2019) and allows direct injection of the point spread function (PSF) into the SMF core. The second approach involves using a photonic lantern (PL) to couple a seeing-limited PSF from the telescope (Leon-Saval et al. 2005; Birks et al. 2015). Acting as a large-core fibre (or waveguide array) at the focal plane, the PL adiabatically transitions a multimode signal input into an equivalent number of SMFs or waveguides. By transforming a multimode input into multiple SMF output, the PL retains the benefits of throughput and minimizing overall instrument size while offering flexibility in spectral formatting, but at the expense of detector real-estate (Harris & Allington-Smith 2012). In particular, this feature allows reformatting of fibres into a pseudo slit, akin to image slicing but using waveguides (Harris et al. 2015; MacLachlan et al. 2017). This pseudo slit may be used to improve stability (Anagnos et al. 2018), improve the utilization of detector pixels, and in certain cases reduce instrument size.

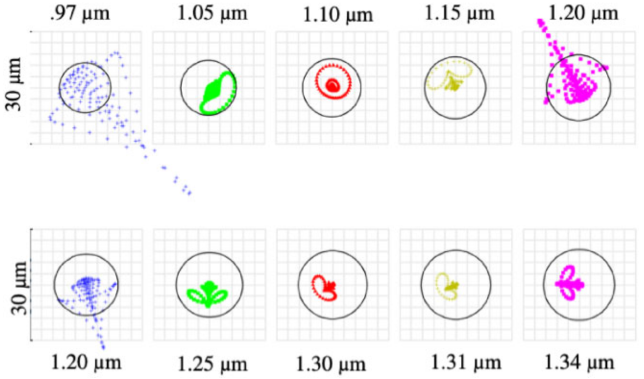

Figure 2. Spot diagrams for both orders of the Lili spectrograph. The first order runs from 0.97 to 1.2 µm and the second from 1.2 to 1.34 µm. In practice the spectrograph is limited by the iLocater fibre link, which accepts 0.97 to 1.31 µm. The spot diagrams are scaled to 30 µm, which corresponds to two pixels on the C-RED 2. For the majority of both orders the light is confined within a two by two square of pixels.

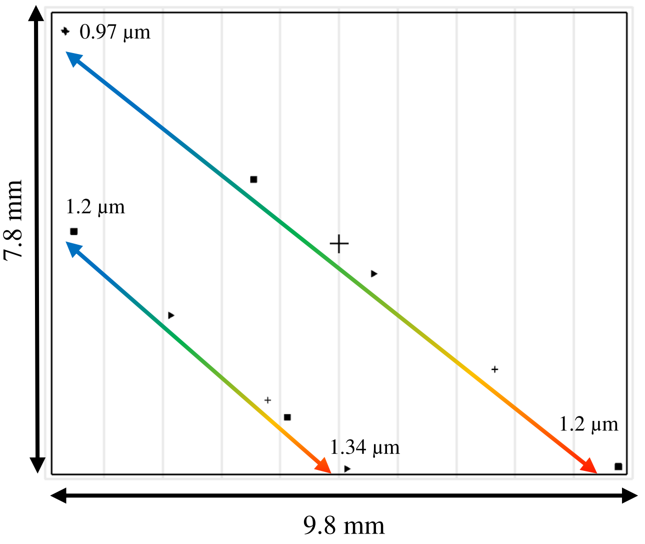

Figure 3. Footprint of the two orders imaged on to the detector. The first order (0.97 to 1.2 µm) crosses the full detector area diagonally, while the second sits below (1.2 to 1.34 µm). Note that there is a difference in slope between the first and second orders due to the rotation of the diffraction gratings.

1.3 The iLocater spectrograph and Lili

iLocater is an AO and SMF-fed, high-resolution, stabilized Doppler spectrograph (Crepp et al. 2016) developed for the dual 8.4 m diameter mirrors of the Large Binocular Telescope (LBT) and is due to be commissioned in 2025. The two telescope beams are received by the Universal Beam Combiner (UBC) of the LBT interferometer (LBTI; Hinz et al. 2016; Ertel et al. 2020) located at the common centre bent Gregorian focus of the two LBT apertures. The two beams are AO corrected by the telescope's adaptive secondary mirrors and the wavefront sensors of the Single-conjugated adaptive Optics Upgrade for the LBT (SOUL) (Pinna et al. 2016). Once operational, iLocater will receive those beams and inject them into two SMFs, each corresponding to ≈40 mas on-sky. The two SMFs, along with a calibration fibre, will feed a cross-dispersed Echelle spectrograph that operates in the *YJ*-bands from 0.97 to 1.31 µm

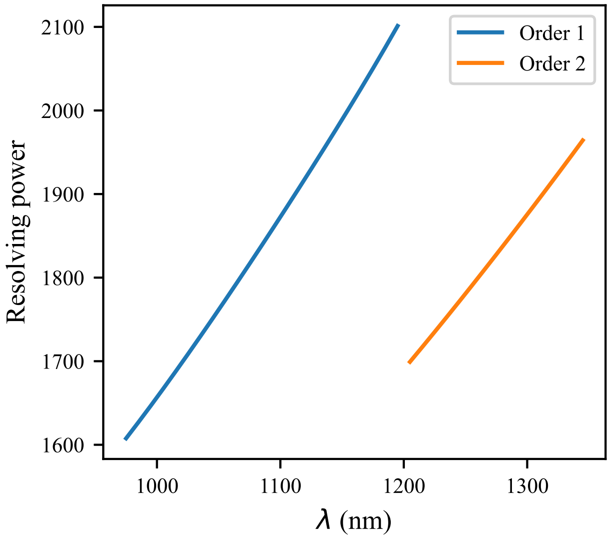

Figure 4. Theoretical resolving power versus wavelength for order one and order two of Lili. This optical design meets the required resolving power of $R = 1500$.

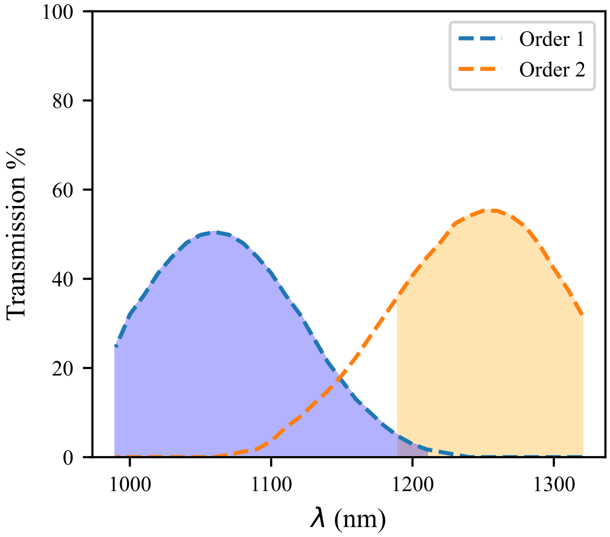

Figure 5. Estimated spectrograph throughput based on commercially available values for lenses and theoretical values for the MCIFU gratings. Individual efficiencies of the two spectrograph orders are plotted as dotted lines. The filled area underneath indicates the parts of the spectrum from each order incident on the C-RED 2 detector.

(Crass et al. 2022). The instrument is designed to deliver high-spectral resolving power $R = \lambda/\Delta\lambda = 125\,000$ to $281\,000$ with a median value of 190 500 and be stabilized to sub-meter-per-second precision. The acquisition camera for the LBT SX (left side) primary mirror has already been installed and tested using narrow-band filters (Crass et al. 2021). To test the acquisition camera performance spectroscopically, we have developed Little iLocater (Lili), a compact miniature spectrograph which was temporarily installed at the LBT to further validate the end-to-end system performance and enables the development operational procedures for the observing modes of iLocater.

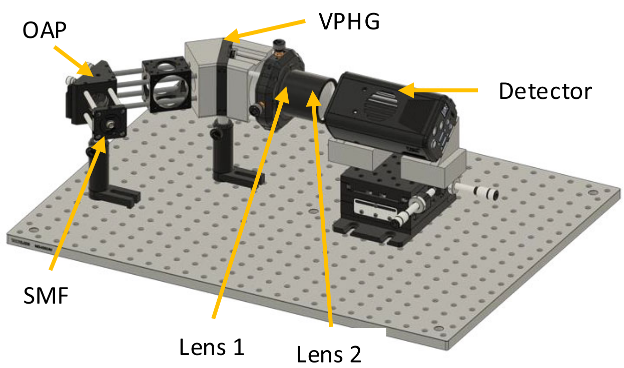

Figure 6. CAD rendering of the Lili spectrograph. On the left, the iLocater SMF that takes light from the acquisition camera injects light into Lili. The light is collimated by the OAP. The cage plates and 3D printed parts ensure the triple stacked VPH grating is correctly angled for dispersion. The dispersed light is finally focused by two lenses onto the C-RED 2 detector.

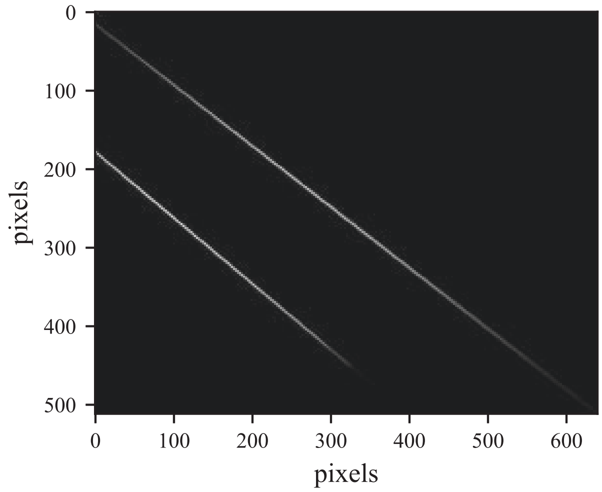

Figure 7. Example raw image of a Halogen spectra taken with the C-RED 2 detector. The two orders are visible: the first order runs across the centre of the image from top left to bottom right (0.97 to 1.2 μm) and the second order is on the bottom left (1.2 to 1.34 μm). Similar images were used to establish the spectral trace for processing.

1.4 Paper outline

In this paper, we describe the first spectral tests of the iLocater front-end fibre-injection system (acquisition camera) using Lili, a shoe-box sized spectrographic precursor to the full iLocater instrument. A low-resolution spectrograph by design, Lili allows validation of the iLocater SX acquisition camera system and atmospheric dispersion corrector (ADC; Crass et al. 2021) prior to integration and commissioning of the final spectrograph (Crass et al. 2022).

In Section 2, we describe the Lili spectrograph, including optical and mechanical design, calibration, and data reduction. In Section 3, we describe the as-built lab performance. In Section 4, we describe on-sky performance at the LBT for a selection of targets. In Section 5, we discuss what improvements could be made to the spectrograph in the future and in Section 6, we provide concluding remarks.

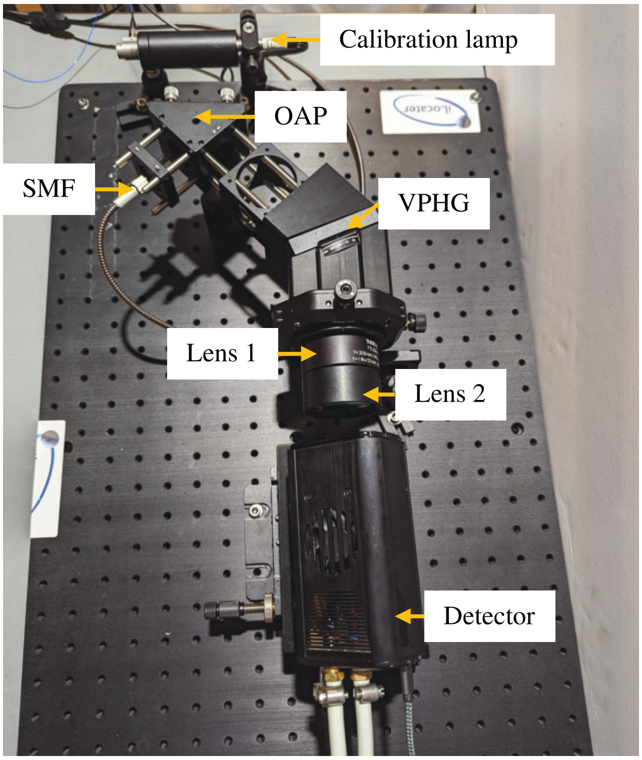

Figure 8. The assembled Lili spectrograph and a calibration lamp on a breadboard at the LBT. At the top of the image an Argon calibration lamp is placed inside a lens tube. An OAP focuses the light into a fibre which is fed through the iLocater system back to the spectrograph. At the bottom of the image (see Fig. 6 for reference), the iLocater SMF that takes light from the acquisition camera injects light into Lili. The light is collimated by the OAP. The cage plates and 3D printed parts ensure the triple stacked VPH grating is at the correct angle for dispersion. The dispersed light is focused by two lenses on to the C-RED 2 detector.

2 LILI

To test iLocaters's acquisition camera and fibre-injection system, Lili was built to accept a wavelength range similar to the final iLocater bandpass $\lambda = 0.97$ to 1.31 µm. Lili was designed to generate a resolving power of $R \approx 1500$, allowing resolution of spectral lines, and to run at speeds of 100 Hz, allowing for real-time analysis of effects such as wavelength-dependent throughput.

To minimize costs for the spectrograph, components from other projects were re-used as the basis for system design and were augmented with commercial off-the-shelf (COTS) components when needed. Three key elements drive the design: the SMF used by the iLocater team, the triple stacked volume-phase holographic (VPH) grating from the Multi-Core Integral Field Unit (MCIFU), and the First Light C-Red 2 InGaAs detector (C-RED 2) detector. Table 1 shows the parameters of the C-RED 2 detector, which has 640 × 512 pixels of 15 µm.

2.1 Optical design

The optical design of Lili is shown in Fig. 1. An SMF injects broadband light into the system. The output of the SMF is modelled as a Gaussian beam, with a $1/e^2$ numerical aperture (NA) = 0.12, which corresponds to the fibre supplied by the iLocater team. As the SMF acts as an on-axis point source, an off-axis parabola (MPD129-P02, Thorlabs) is used to provide a collimated beam. The collimated light feeds a spare triple stacked VPH grating (VPHG) from the MCIFU spectrograph (Haffert et al. 2020). The grating, which is set at 21° to the beam, is slightly off the design angle of 22°, reducing efficiency by approximately 8 per cent. The grating is composed of three gratings, nominally rotated at 3° with respect to each other, allowing separation of three orders on the detector. The resulting diffraction

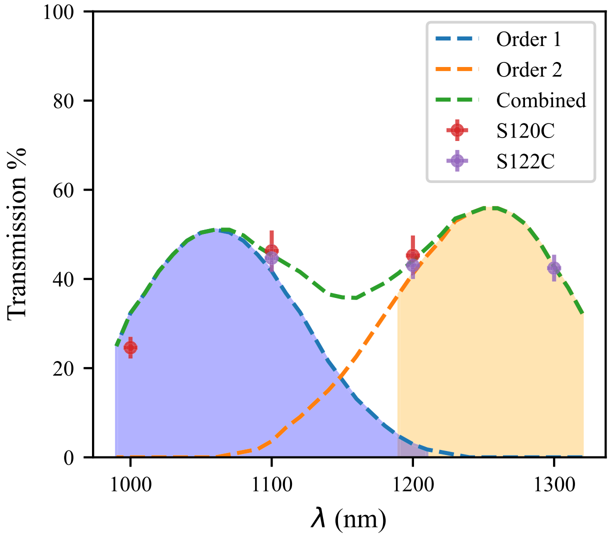

Figure 9. The transmission of Lili at the LBT versus the theoretical transmission (see Fig. 5). The values are measured using filters with a 10 nm full width half-maximum (FWHM), supercontinuum source and power meter. Note that due to the large power meter area we measure the combined power from both orders simultaneously (the combined theoretical line). The difference (≈3 per cent) between the two measurements at 1200 nm is ascribed to the low efficiency of the S120C power meter at this wavelength and is within the quoted error from the vendor.

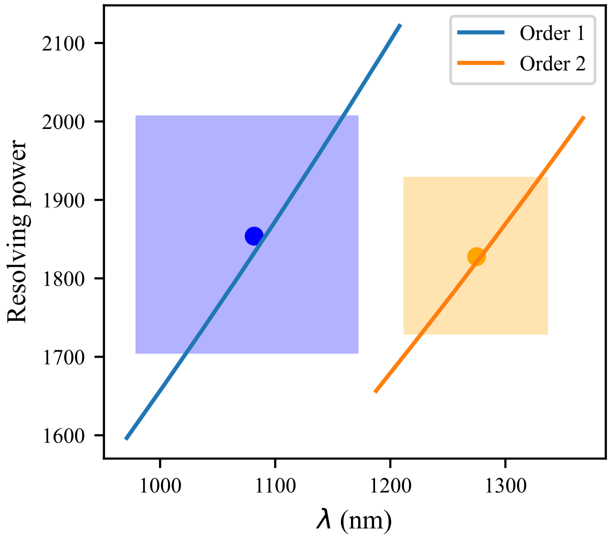

Figure 10. Calculated resolving power of the as-built Lili spectrograph, with order one on the left and order two on the right. The shaded box shows the 1σ resolving power estimates from the Argon emission lines within each order. The points within the box show the median resolving power of that order. We also overplot the resolving power from the design values, showing good agreement.

Table 2. Table of observations, conditions, and detector parameters for Lili observations. Target magnitudes are taken from Simbad. The natural seeing is measured using the DIMM at the LBT using a bright star within 25° of the target star. The frame rate and gain are for the C-RED 2. The test column lists hardware that was being tested.

Target	J (mag)	DIMM Seeing (arcsec)	Frame rate (Hz)	Gain	Test
Vega	−0.177	0.7–1.4	100	low	Spectrograph
Arcturus	−2.252	0.8–1.2	100	low	Spectrograph
27 Her	0.858	1.3–2.5	100	high	ADC
41 Vir	5.7	0.8–1.2	2	high	AO

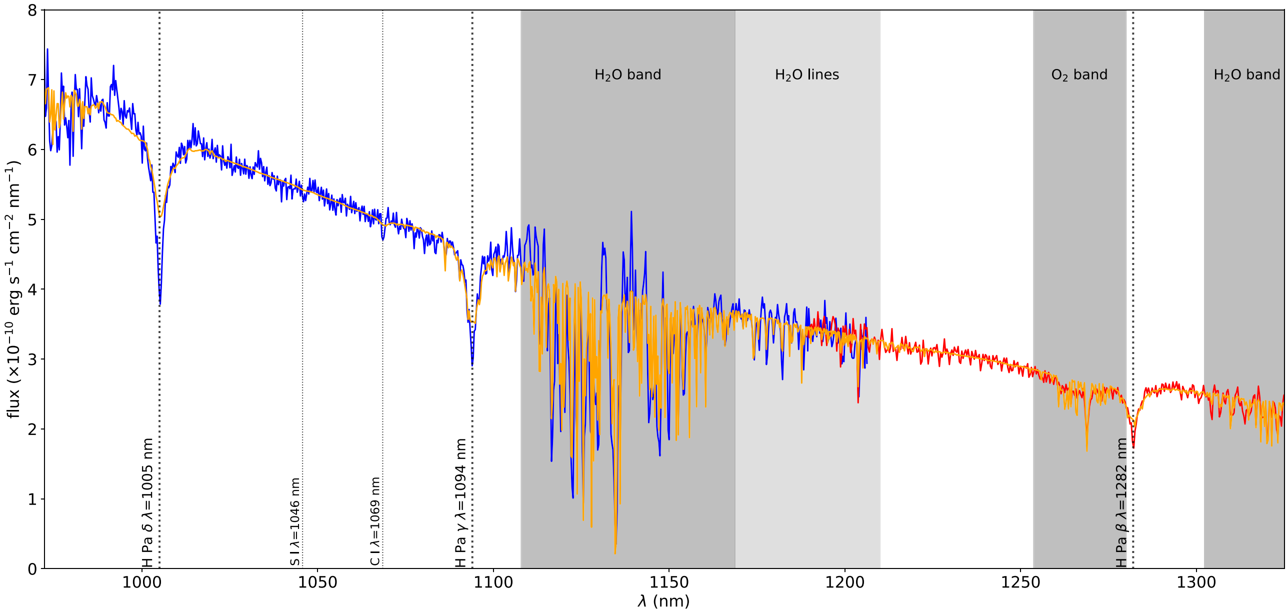

Figure 11. Spectrum of *Vega* recovered by the Lili spectrograph overplotted with a synthetic model. Order one is shown in blue (left side), order two is shown in red (right side), and the synthetic model is shown in orange. Stellar and telluric features are annotated on the plot. Overall, Lili recovers the spectral features of *Vega* in both orders.

pattern is then re-imaged using two lenses, a TTL200-S8 (Lens 1 in Fig. 1) and AC-508-080-C (Lens 2 in Fig. 1), both from Thorlabs. Unlike the MCIFU, wavelengths longer than approximately 1.31 μm are not transmitted through the iLocater fibre injection system, thus only two of the three VPH gratings are used. It should be noted that the grating was designed to eventually be used with a HAWAII-2 detector and in this system we reduce the image size by a factor of approximately four to fit on to the smaller C-RED 2. This reduced the spectral resolving power of the system because of undersampling of the line spread function (LSF), which is discussed further in Section 4.

2.1.1 *Lili resolving power*

Fig. 2 shows the resulting spot diagram on the detector for wavelengths of the two orders incident on the C-RED 2. With the exception of the edges of each order, all of the resulting spots are smaller than the Airy radius. In physical units, the images spots are less than 30 μm in diameter corresponding to two pixels on the C-RED 2. From the Nyquist–Shannon theorem, Lili is undersampled on the detector and in the ideal case of perfect alignment the resolving power will be limited by the pixel size, not image quality.

In order to maximize resolving power, while also maximizing wavelength coverage, the C-RED 2 is rotated by a slight angle, placing the longest order (order one) diagonally from corner to corner (see Fig. 3). By doing so, this gives a theoretical resolution of ≈1600 to 2100 for order one and ≈1700 to 2000 for order two (see Fig. 4).

2.1.2 *Theoretical spectrograph transmission*

The spectrograph transmission was estimated using commercially available values for the lenses and OAP from Thorlabs, the quantum efficiency (QE) numbers for the C-RED 2 from First Light and the efficiency numbers for the gratings measured by the MCIFU team, including a factor to account for the grating being used off of its design wavelength. As the Zemax model showed no vignetting in the optical design, no additional factors were added. The transmission across the Lili wavelength range is shown in Fig. 5. A peak transmission of ≈50 per cent is reached in each order, consistent with the MCIFU.

2.1.3 *Optical sensitivity*

A sensitivity study of the optical components was performed in ANYSYS Zemax to evaluate the feasibility of the Lili design. Alignment of individual elements was allowed to vary by 0.2 μm and 0.2°, with focus adjustment of the detector acting as a free parameter to compensate and improve image quality. The energy contained in one pixel for wavelengths in the first order (0.97 to 1.2 μm) was used as a metric for evaluation. The most sensitive

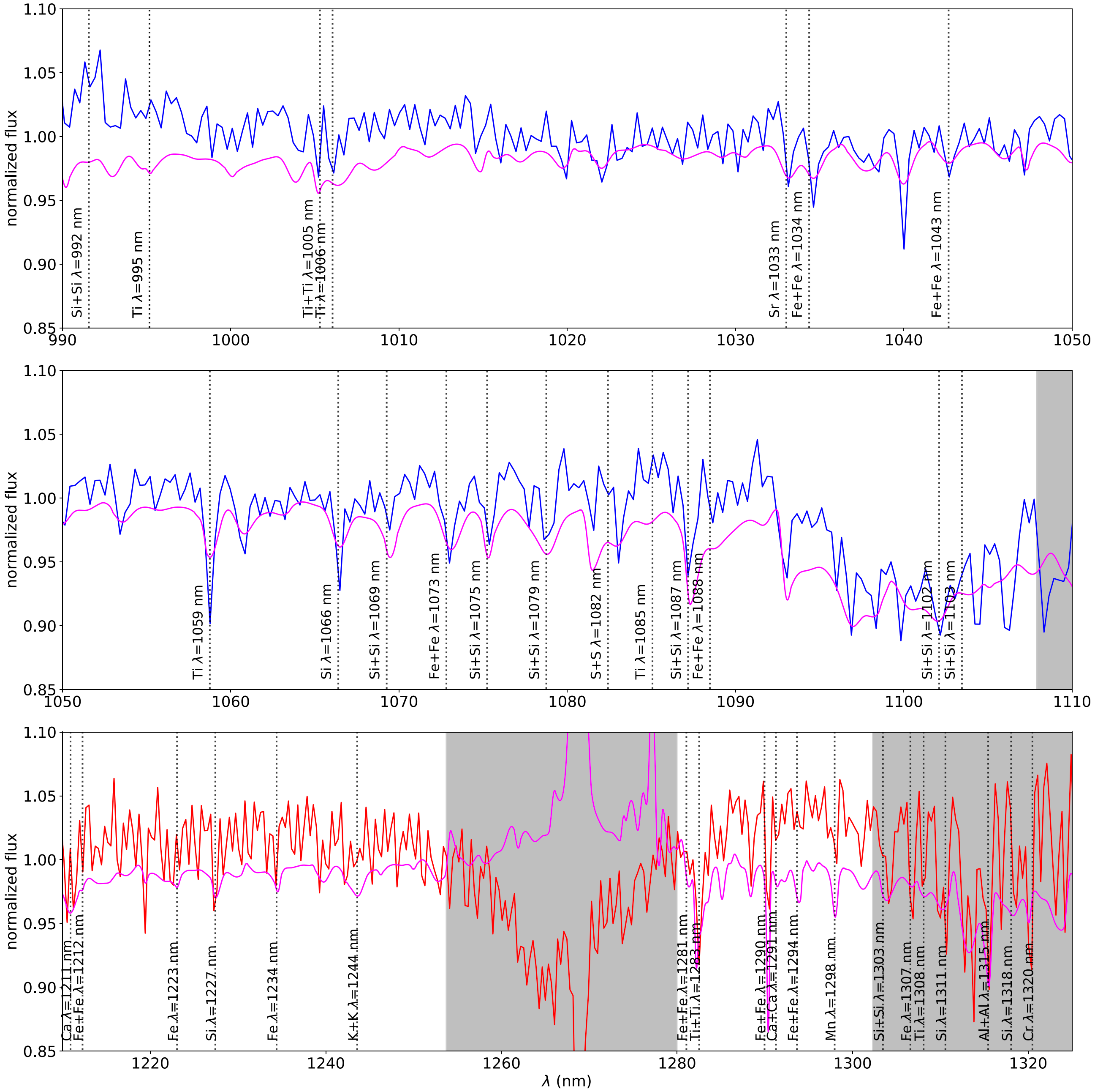

Figure 12. Spectrum of *Arcturus* from Lili (blue and red showing the two orders) compared to a reference spectrum of *Arcturus* from Hinkle et al. (1995), convolved with an approximation of the Lili line spread function (pink). Line identifications are shown with the vertical dotted lines, labelled with the species and wavelength, from Hinkle et al. (1995). Although there are still imperfections in the continuum normalization of the Lili spectra, even subtle features in these spectra match real lines in the reference spectrum.

element was found to be the OAP, with x and y centering reducing energy by 50 per cent; tip/tilt of the OAP contributed ≈1 per cent reduction in enclosed energy. All other elements in the spectrograph had less than 1 per cent influence on the amount of light contained within one pixel and were considered negligible.

2.2 Mechanical design

A CAD rendering of the Lili spectrograph is shown in Fig. 6. The system relies on cage mounts and rods for mechanical alignment and rigidity. As Section 2.1.3 already demonstrated, the OAP alignment is critical and thus the OAP was mounted in a fine adjustment mount (Thorlabs KCB1P/M). As with the MCIFU, two holders were printed in polylactic acid (PLA) to hold the VPH grating at the correct angle. Experience with the MCIFU had shown that having accessible rotation adjustment for the VPH gratings simplified alignment, so a custom rotation adapter was manufactured and placed inside a LCRM2A/M from Thorlabs. For ease of co-alignment, the two lenses are placed in a lens tube and mounted on an x–y stage (CXY2A, Thorlabs). The C-RED 2 is liquid cooled to reduce dark current is also placed on an x–y stage to allow focus and horizontal position optimization.

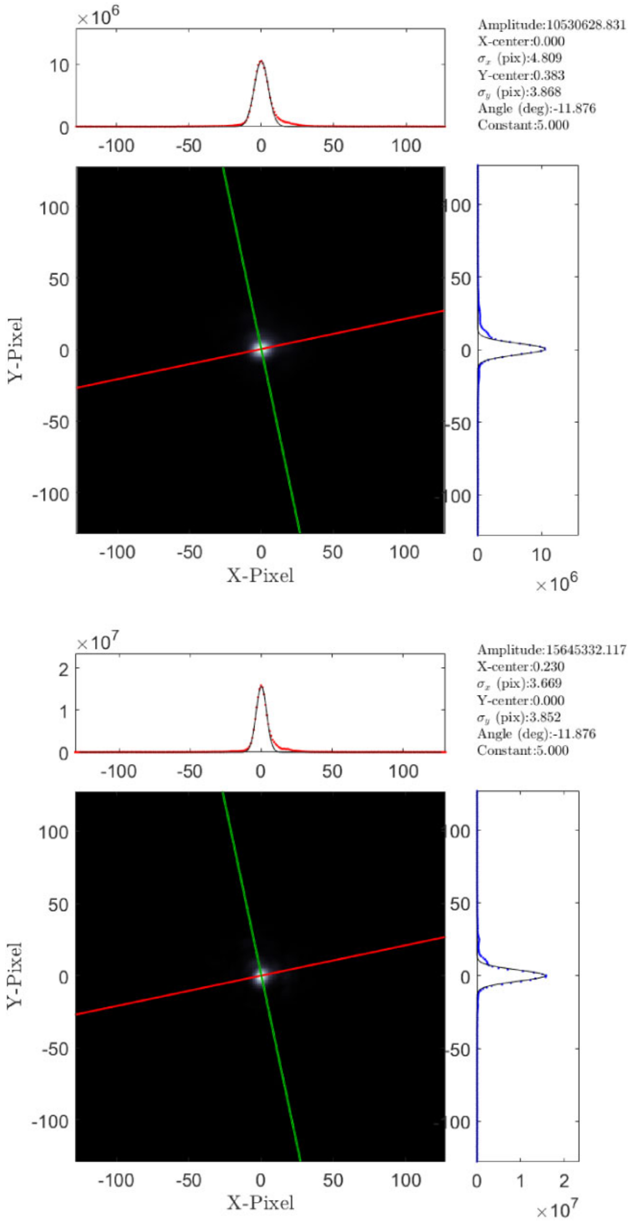

Figure 13. Images of 27 *Her*, recorded in the iLocater imaging channel. The images have two dimensional Gaussians fitted, with the x-axis set to be along the atmospheric dispersion direction. (Upper) Image of 27 *Her* with the ADC set to null position. The calculated standard deviation for the Gaussian is 4.8 pixels in the x direction compared to 3.9 in the y direction. (Lower) Image of 27 *Her* with the ADC on. The calculated standard deviation for the Gaussian is 3.7 pixels in the x direction and 3.9 in the y direction.

2.3 Calibration and data reduction

Several different light sources were used for alignment and calibration. Initial alignment was performed using a 1060 nm laser (S1FC1060, Thorlabs), and a Halogen lamp (OSL2IR, Thorlabs) was used to align the spectrograph orders to the detector (see Fig. 7 for an example). A supercontinuum source (WhiteLase Micro, Fianium) was used with narrow-band filters (FKBIR kit, Thorlabs) to ensure that the wavelength range was correctly covered. A filter kit was also used to measure transmission across the desired wavelength range (see Section 3.1). The fully assembled spectrograph was flat-fielded using the halogen lamp and wavelength calibration was performed using an Argon pencil lamp (6030, Newport).

We extracted spectra using standard processing steps, with a custom PYTHON implementation. Extraction proceeded separately for each of the two spectral orders, which were combined into a single FITS file at the end. The spectral orders have negligible curvature but the dispersion direction is rotated at an angle of 38° for order one and 40° for order two with respect to the rows of the detector. This is 1° less than the nominal design in rotation (3°, see Section 2.1). As the spectral orders are well separated this has no impact. We rectified this rotation with a simple rotational interpolation to align the dispersion with the columns. We used the optimal extraction algorithm (Horne 1986) to produce a 1D spectrum, using the Halogen lamp spectrum to compute the spectral profile necessary to extract the science spectra. This profile was used to perform optimal extraction of science spectra.

We computed the wavelength solution in two steps. First, we used spectra obtained through the series of narrow-pass filters to create a rough wavelength solution. Second, we extracted a spectrum from the Argon lamp. We identified the Ar peaks, and used the rough wavelength solution to match the peaks to an Ar line list sourced from NIST; several lamp lines not present in the Ar line list were discarded by hand. A quadratic fit to the expected wavelengths versus measured pixel positions of the lines produced a wavelength solution with a dispersion of 0.03 nm in order one and 0.05 nm in order two.

We removed the blaze function and normalized the continuum in a two-step process. First, we divided the spectra by the Halogen flat lamp spectra. This mostly removed the blaze function, as well as a component of high-frequency noise due to stripping in the C-RED 2. As the shape of the flat lamp spectrum is not the same as the observed spectra, there is still a low-order shape to the blaze-corrected spectrum. We removed the low-order shape by performing an iterative spline fit to the data, rejecting points well below and above the continuum in order to remove absorption lines and isolate the continuum.

Finally, we performed a flux calibration on the extracted spectrum using Vega as a reference. We built a synthetic model from Caloec (Bohlin, Gordon & Tremblay 2014) convolved with the ESO SKYCALC atmospheric transmission model (Noll et al. 2012; Jones et al. 2013; Moehler et al. 2014) and interpolated it to the data. The data are divided by the model to get the ratio of flux. We smooth this ratio using a 3rd order Savitzky–Golay filter, with a window length of 200 pixels. The data are then multiplied by the flux ratio to retrieve the flux calibrated spectrum.

3 ON-SKY TESTING AT THE LARGE BINOCULAR TELESCOPE

Assembly, characterization, and on-sky testing of Lili with the iLocater acquisition camera took place in May 2024. We were allocated two half nights for on-sky tests, which required median-seeing conditions or better to allow efficient AO system operation.

Lili was assembled inside the telescope pier on level 3L, where iLocater will eventually be located. The fibres that will feed iLocater were already installed. The C-RED 2 was attached to the LBT chilled water system and was cooled to −40° C for all of the tests. An annotated image of the as-built spectrograph can be seen in Fig. 8. The spectrograph is built on an aluminium breadboard, with vibration damping feet (AV5, Thorlabs) and placed in an enclosure to minimize stray light entering the system. Temperature control and vibration reduction measures that will be used with iLocater were not in place during this visit. To minimize any

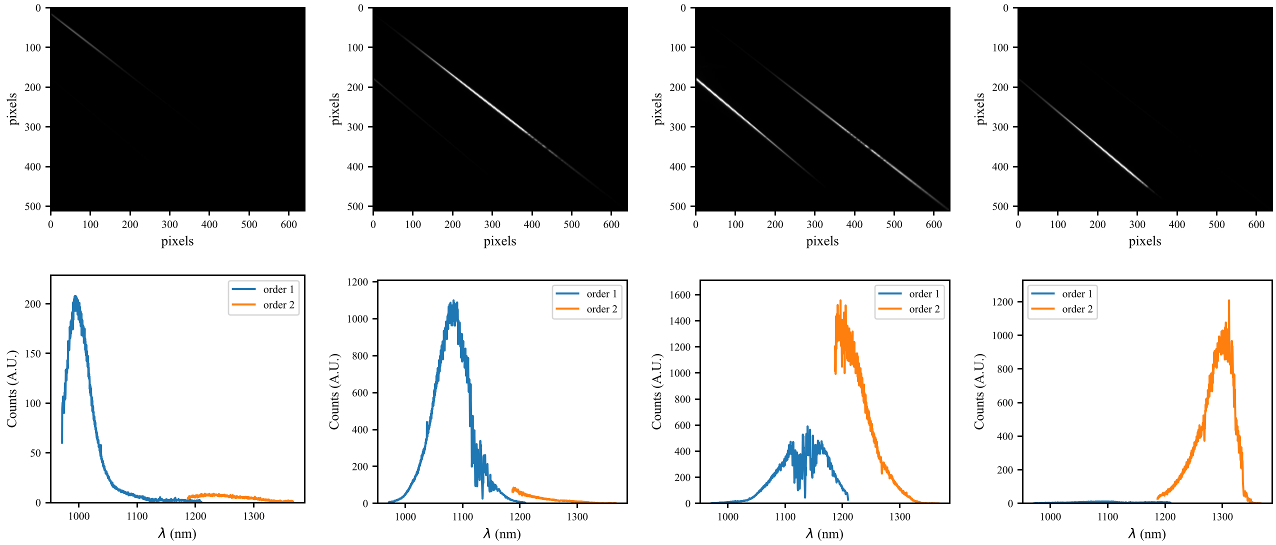

Figure 14. Raw frames (top) and extracted spectra (bottom) of 27*Her* from Lili. The four images are of spectra taken with the ADC in null position, with the SMF being scanned along the atmospheric dispersion direction. As the fibre is scanned, the peak flux changes from the shortest wavelengths (top left in image, left in graph) to the longest (bottom right in image, right in graph).

potential impact from people changing the temperature or causing vibrations, Lili was operated remotely from the telescope control room.

3.1 Lili measured transmission

The transmission of the spectrograph was measured by illuminating the input fibre with the iLocater supercontinuum source. The light was filtered using 10 nm bandpass filters (FKBIR kit, Thorlabs) located in the collimated beam before the VPH grating. The power from the fibre input to the spectrograph and the power at the detector was measured using two separate power meter sensors (S120C and PM16-122, Thorlabs) to cover the whole bandpass. The ratio of the output power against the input power was then taken, giving the transmission of the spectrograph. It should be noted that the measured power was a combination of both spectral orders.

Results are shown in Fig. 9 and show very good agreement with the expected transmission from Fig. 5. There is a discrepancy of up to 3 per cent between the transmission measured by the two power meters at the overlap point; this is ascribed to the sensor measurement accuracy at these wavelengths, which is quoted as 7 per cent and 5 per cent from the vendor specifications.

3.2 Order size and measured resolving power

To estimate the magnification of the system we use the known Gaussian $1/e^2$ mode-field diameter (MFD) values from Crass et al. (2021). For order one the supplied fibre has a $1/e^2$ MFD of 5.8 µm at 980 nm, increasing to $\approx$ 7 µm by 1200 nm. For order two this is $\approx$ 7 µm at 1200 nm increasing to $\approx$ 7.8 µm at 1310 nm. To calculate the output, we fitted a Gaussian to the spectrally flattened LSF of each order and calculate the average $1/e^2$ value of each order. This is calculated as 43 µm in order one and 34 µm in order two. We estimate the magnification as 6.14–7.4 for order one and 4.4–4.8 in order two. This indicates that order one was slightly defocused when compared to the design, likely due to a tilt on the detector stage.

The resolving power of the as-built spectrograph was estimated using the spectra of the Argon lamp. We used the calculated parameters of the emission lines, converting the standard deviation of the fitted Gaussian to the FWHM; this number was rounded up to an integer number of pixels. The resolving power was then estimated using $R = \lambda/\delta\lambda$. The results are shown in Fig. 10, with order one shown in blue and order two shown in orange. The shaded box shows the 1σ resolving power estimates from the Argon emission lines and the points within the box show the median resolving power of that order. The measured resolving power shows good agreement with the design.

4 TESTING ON-SKY

On-sky testing at the LBT occurred between 0:00-05:30 and 18:30-24:00 local time (UT-7) on 2024 May 17 in two half night blocks. A selection of the observed targets are listed in Table 2. *Vega* and *Arcturus* were chosen as they were both high in the sky and already well-characterized by other instruments; they provided validation for the spectrograph measurements. *27 Her* was chosen to test the ADC performance given its brightness and low elevation. Finally, *41 Vir* is a known close-companion system and at the time of observation was estimated to have a separation of ≈50 mas; it was chosen to test the ability of the iLocater SX acquisition system to isolate and record individual spectra of close companions.

4.1 Spectral extraction: *Vega* and *Arcturus*

Observations of *Vega* and *Arcturus* allowed the C-RED 2 to run at 100 Hz at low gain given the brightness of the targets. The reduced spectra were used to provide calibration for Lili and test the data reduction pipeline.

The extracted spectra of *Vega* is shown in Fig. 11. The data were reduced as described in Section 2.3. We were able to identify several expected lines (H Pa δ, H Pa γ, H Pa β), as well as potential metal lines from Si I and C I.

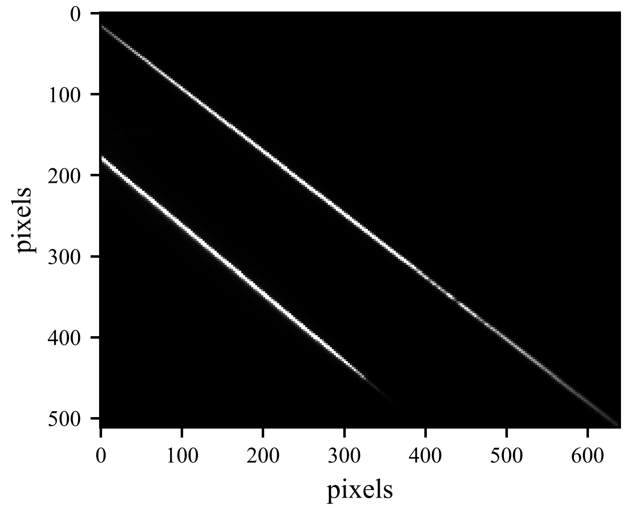

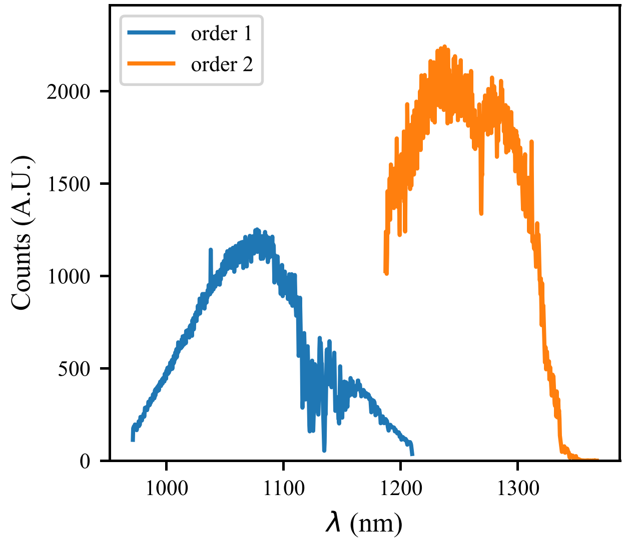

Figure 15. Raw frames and extracted spectra of *27 Her*, with the ADC set to compensate for chromatic dispersion due to elevation. Here the blaze function of the spectrograph is clearly visible in both orders, but there is flux across the whole iLocater bandpass.

To estimate the flux coming from iLocater acquisition camera performance we chose 1050 nm as our zero-point. Integrating across the spectra over a 1 nm provides approximately 1000 ADU, which at low gain converts to $8.5 \times 10^5\,e^-$ or 1.2×10^7 phs^{-1} nm^{-1} at the detector.

We also compared the spectrum of *Arcturus* to a reference spectrum from Hinkle, Wallace & Livingston (1995) (Fig. 12). This spectrum was obtained with the Fourier transform spectrometer at Kitt Peak, at a resolution considerably higher than what Lili delivers; we therefore convolved this spectrum with a Gaussian function approximating the Lili line spread function for a better comparison with our data. We find the data to have a signal to noise of ≈20, due to read noise, dark current, and the integration time, which matches our estimations well. Despite this the results of the convolution suggest that we have detected many actual lines in the spectrum and the degree of systematic noise is low.

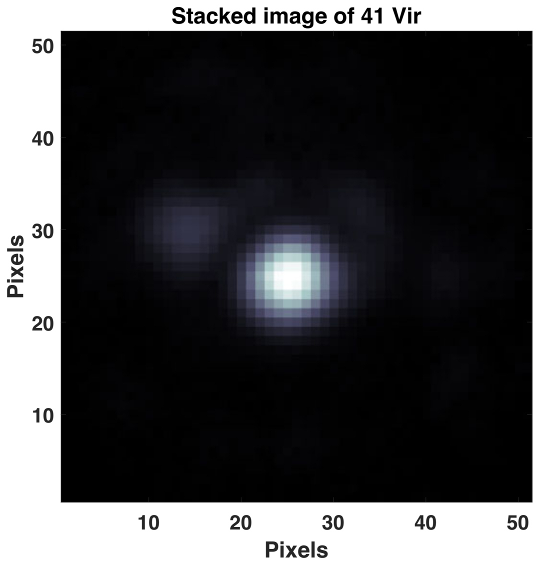

Figure 16. Image of the *41 Vir* system taken with the imaging arm of the iLocater acquisition camera. Here the primary component is clearly visible, with the secondary much fainter above and to the left. Note the distance between the two components is ≈50 mas.

4.2 ADC testing

Previous testing of the ADC within the iLocater acquisition camera (Kopon et al. 2013) had only been completed using the imaging channel (Crass et al. 2021). Lili allowed this to be expanded to detailed characterization across the full iLocater bandpass. The target *27 Her* was used for testing which has a $J_{\rm mag} \approx 1$. While this is a known spectroscopic binary system, its semimajor axis of 11 mas is below the spatial resolution limit of iLocater and the LBT. During observations, *27 Her* was at an elevation of $\approx 40^\circ$ allowing measurable dispersion to be present in both the imaging and spectroscopic channels. Initially the ADC was set to its null position (no correction), leading to a dispersed PSF within the acquisition camera (see Fig. 13, upper). To ensure the dispersion was due to the lack of ADC correction, we optimized fibre coupling at the shortest wavelength ($\lambda = 0.97$ μm and then the iLocater SMF was physically scanned across the focal plane in the atmospheric dispersion direction in a series of steps. Moving the SMF by 31 μm moved the peaked flux from the blue to the red end of the spectrum ($\lambda = 1.31$ μm). The results of the stepping procedure on the spectra are shown in Fig. 14. Subsequently, ADC correction was enabled within the acquisition camera (see Fig. 13, lower) and the expected full *27 Her* spectra was recovered by Lili (see Fig. 15).

4.3 Spatially resolved close companions

The system *41 Vir* (HD 112097) was observed as it is a known double-line spectroscopic binary system, with radial velocity measurements having been made previously (Grandjean et al. 2021). The separation of the two companion stars (∼50 mas) means it is difficult to acquire separate spectra of the individual components and the authors have not found any such spectra in the literature. Our observations thus focused on producing the first spatially resolved spectra of the system. With the telescope AO loop closed, the acquisition camera was used to position the SMF on to the primary component of the system and spectra were recorded using Lili. The fibre was then repositioned on to the second component with spectra again being

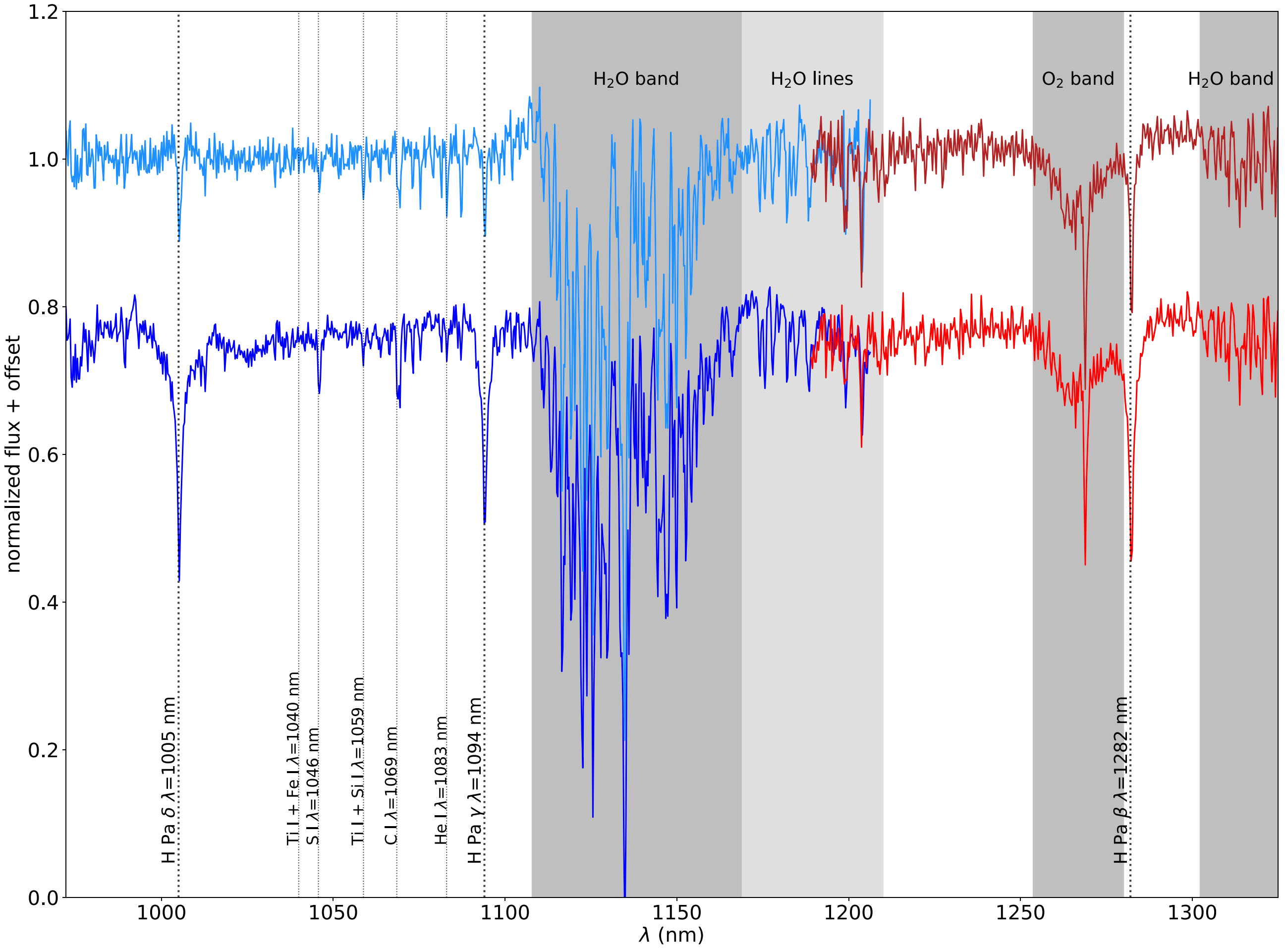

Figure 17. Spectra of the primary component of *41 Vir* (bottom) and the 50 mas companion (top), vertically offset for clarity. The two Lili orders are plotted in blue and red, respectively. Notable spectral lines and bands are marked.

recorded (see Fig. 16). The resulting spectra are shown in Fig. 17, with the two *41 Vir* components being separated by an offset. The differences in the H Pa δ and γ are clearly visible in the plot and we appear to see more metal lines in the 1050 to 1100 nm region in the cooler star, showing that we are observing two different stars.

5 FUTURE OPTIMIZATION OF LILI

The optical and mechanical components of Lili functioned as expected, providing a resolving power of $R \approx 1500$ for the iLocater bandpass. Despite this, as discussed in Section 2.1 and shown in Fig. 3, Lili does not make optimal use of the C-RED 2 detection area, nor utilize the full resolving power of the grating. It is unlikely that Lili will be used for further validation of the iLocater acquisition camera before commissioning in the current timeline. However the design for Lili provides a good foundation for future experiments, so improvements are worthwhile considering.

5.1 Changes to the detector

To allow optimal sampling while retaining the same C-RED 2 detector a similar approach to the MCIFU could be taken (Haffert et al. 2020). This would involve removing the second lens, increasing the size of the image and moving the C-RED 2 using two linear stages to cover the whole bandpass. For the tests in this paper, this was not an option as we wished to cover the whole iLocater bandpass simultaneously, but for other experiments could provide the whole bandpass at a higher resolving power. Alternatively a detector with more pixels (such as a HAWAII-2) could be purchased, allowing the whole field to be covered simultaneously. This would no longer allow the same frame rate as the C-RED 2, but would have lower noise and higher QE.

5.2 Image slicing to optimize detector use

To efficiently fit the spectrum from Lili on to the C-RED 2 detector an image slicer could be used. Image slicers are typically used as a integral field units (IFUs; Calcines, López & Collados 2013) to reorganize a 2D field of view into one or more slits that illuminate a spectrograph, thereby obtaining the spectra of all spatial elements simultaneously. Image slicers can also be found at a pupil position (Roelfsema et al. 2018) (pupil slicer) or as a field reformatter (Calcines et al. 2023) before the spectrograph. We investigated using an image slicer to slice the output spectrum and image it on the detector. The investigation revealed a number of problems with this approach and it was decided this would be too costly and difficult to implement. In the future we plan to investigate alternative solutions, like the use of an array of slicer mirrors to decompose the spectrum and correct its tilt angle, combined with lenses to fit the spectra on the detector. These lenses will be optimized for their correspondent wavelengths, reducing the volume required for spectrum slicing.

6 CONCLUSIONS

The results presented in this paper show the first spectral characterization of the iLocater acquisition camera at the LBT. To achieve them we designed, built, and tested Lili, an SMF-fed spectrograph covering the iLocater wavelength range 0.97 μm to 1.31 μm with a resolving power between 1500 to 2100. The resolving power and transmission of the as-built spectrograph matched the design.

The tests detailed in this paper and previously (Crass et al. 2021) are key to ensuring an efficient commissioning process for iLocater. By studying bright stars at high frame rates, we were able to record and extract spectra across the full iLocater passband which is consistent with prior data in the literature. Our ADC tests show good performance at elevations of 40°, which is the approaching the operational limit for the ADC and telescope AO system (Crass et al. 2021). This complements and extends the confidence that during commissioning, that iLocater will be able to push to the lower limit elevation of 30°. We believe our spectra are the first spatially resolved spectra of *41 Vir* A and B. In acquiring them, we have demonstrated the ability of the acquisition camera to spectrally separate close-separation systems (≈50 mas) and such a proven capability will help define early science targets for iLocater and subsequent studies.

As this and previous papers have shown, the facilities at the LBT and the iLocater acquisition camera provide an excellent platform to test new technologies and techniques (Hottinger et al. 2021). Future testing with this system include the commissioning of iLocater and the full optimization of the acquisition camera. As this platform also enables the demonstration of photonic technologies in astronomical instrumentation, such as photonic beam stabilization technologies, photonic spectrographs or novel types of IFUs, it can play an important role in their timely advancement. This will help augment diffraction-limited on-sky capabilities in an efficient way, and deliver science capabilities on an accelerated timeline.

ACKNOWLEDGEMENTS

RJH would like to thank all that have indirectly contributed to the project. In particular André Boné for his optical design input and the MCIFU team for their work designing the MCIFU, inspiring this spectrograph. He wants to thank Mark Swinbank and Daniel J. Stevens for discussions on astronomical targets and spectra. He also wishes to thank Lazar Staykov, the support team at the LBT and the L3 lab technicians Durham University, without whom this would not have worked out.

MCJ thanks Jennifer Johnson and Adam Wheeler for useful discussions on line identification and spectral synthesis. He also acknowledges support from the Thomas Jefferson Endowment for Space Exploration.

The LBT is an international collaboration among institutions in the United States, Italy, and Germany. LBT Corporation Members are: The University of Arizona on behalf of the Arizona Board of Regents; Istituto Nazionale di Astrofisica, Italy; LBT Beteiligungsgesellschaft, Germany, representing the Max–Planck Society, The Leibniz Institute for Astrophysics Potsdam, and Heidelberg University; The Ohio State University, representing OSU, University of Notre Dame, University of Minnesota and University of Virginia.

Observations have benefitted from the use of ALTA Center (alta.arcetri.inaf.it) forecasts performed with the Astro-Meso-Nh model. Initialization data of the ALTA automatic forecast system come from the General Circulation Model (HRES) of the European Centre for Medium Range Weather Forecasts.

This material is based upon work supported by the National Science Foundation under Grant No. 1 654125 and 2108603.

This research made use of ASTROPY, a community-developed core PYTHON package for Astropy Collaboration (2013); Price-Whelan et al. (2018), NUMPY Harris et al. (2020), SCIPY Virtanen et al. (2020), and MATPLOTLIB Hunter (2007).

DATA AVAILABILITY

The data and spectroscopic reduction pipeline underlying this article will be shared on reasonable request to the corresponding author.

REFERENCES

Anagnos T. et al., 2018, MNRAS, 478, 4881
Astropy Collaboration, 2013, A&A, 558, A33
Bechter A. J., Bechter E. B., Crepp J. R., King D., Crass J., 2018, in Evans C. J., Simard L., Takami H., eds, Proc. SPIE Conf. Ser. Vol. 10702, Ground-based and Airborne Instrumentation for Astronomy VII. SPIE, Bellingham, p. 107026T
Bechter E. B., Bechter A. J., Crepp J. R., Crass J., 2019, J. Astron. Telesc. Instrum. Syst., 5, 038004
Bechter A. J., Bechter E. B., Crepp J. R., Ketterer R., Crass J., 2020, PASP, 132, 095001
Birks T. A., Gris-Sánchez I., Yerolatsitis S., Leon-Saval S., Thomson R. R., 2015, Adv. Opt. Photonics, 7, 107
Bland-Hawthorn J., Horton A., 2006, in McLean I. S., Iye M., eds, Proc. SPIE Conf. Ser. Vol. 6269, Ground-based and Airborne Instrumentation for Astronomy. SPIE, Bellingham, p. 62690N
Bohlin R. C., Gordon K. D., Tremblay P.-E., 2014, PASP, 126, 711
Calcines A., López R. L., Collados M., 2013, J. Astron. Instrum., 02, 1350009
Calcines A., Wells M., O'Brien K., Morris S., Seifert W., Zanutta A., Evans C., Di Marcantonio P., 2023, Exp. Astron., 55, 267
Crass J. et al., 2019, BAAS, 51, 122
Crass J. et al., 2021, MNRAS, 501, 2250
Crass J. et al., 2022, in Evans C. J., Bryant J. J., Motohara K., eds, Proc. SPIE Conf. Ser. Vol. 12184, Ground-based and Airborne Instrumentation for Astronomy IX. SPIE, Bellingham, p. 121841P
Crepp J. R., 2014, Science, 346, 809
Crepp J. R. et al., 2016, in Proc. Spie, Ground-based and Airborne Instrumentation for Astronomy VI. p. 990819
Ertel S. et al., 2020, in Tuthill P. G., Mérand A., Sallum S., eds, Proc. SPIE Conf. Ser. Vol. 11446, Optical and Infrared Interferometry and Imaging VII. SPIE, Bellingham, p. 1144607
Gibson R. K., Oppenheimer R., Matthews C. T., Vasisht G., 2019, J. Astron. Telesc. Instrum. Syst., 6, 011002
Grandjean A. et al., 2021, A&A, 650, A39
GRAVITY Collaboration, 2017, A&A, 602, A94
Haffert S. Y. et al., 2020, J. Astron. Telesc. Instrum. Syst., 6, 045007
Harris R. J., Allington-Smith J. R., 2012, MNRAS, 428, 3139
Harris R. J. et al., 2015, MNRAS, 450, 428
Harris C. R. et al., 2020, Nature, 585, 357
Hinkle K., Wallace L., Livingston W., 1995, PASP, 107, 1042
Hinz P. M. et al., 2016, in Malbet F., Creech-Eakman M. J., Tuthill P. G., eds, Proc. SPIE Conf. Ser., Vol. 9907, Optical and Infrared Interferometry and Imaging V. SPIE, Bellingham, p. 990704
Horne K., 1986, PASP, 98, 609
Hottinger P. et al., 2021, J. Opt. Soc. Am. B, 38, 2517
Hunter J. D., 2007, Comput. Sci. Eng., 9, 90

Jones A., Noll S., Kausch W., Szyszka C., Kimeswenger S., 2013, A&A, 560, A91

Jovanovic N. et al., 2017, A&A, 604, A122

Kervella P. et al., 2003, in Traub W. A., ed., Proc. SPIE Conf. Ser. Vol. 4838, Interferometry for Optical Astronomy II. SPIE, Bellingham, p. 858

Kopon D., Close L. M., Males J. R., Gasho V., 2013, PASP, 125, 966

Le Bouquin J.-B. et al., 2011, A&A, 535, A67

Leon-Saval S., Birks T., Bland-Hawthorn J., Englund M., 2005, Opt. Lett., 30, 2545

Lovis C. et al., 2022, in Evans C. J., Bryant J. J., Motohara K., eds, Proc. SPIE Conf. Ser. Vol. 12184, Ground-based and Airborne Instrumentation for Astronomy IX. SPIE, Bellingham, p. 121841Q

MacLachlan D. G. et al., 2017, MNRAS, 464, 4950

Mawet D. et al., 2022, in Evans C. J., Bryant J. J., Motohara K., eds, Proc. SPIE Conf. Ser. Vol. 12184, Ground-based and Airborne Instrumentation for Astronomy IX. SPIE, Bellingham, p. 121841R

Moehler S. et al., 2014, A&A, 568, A9

Noll S., Kausch W., Barden M., Jones A. M., Szyszka C., Kimeswenger S., Vinther J., 2012, A&A, 543, A92

Pinna E. et al., 2016, in Marchetti E., Close L. M., Véran J.-P., eds, Proc. SPIE Conf. Ser. Vol. 9909, Adaptive Optics Systems V. SPIE, Bellingham, p. 99093V,

Price-Whelan A. M. et al., 2018, AJ, 156, 123

Roelfsema R. et al., 2018, in Evans C. J., Simard L., Takami H., eds, Proc. SPIE Conf. Ser. Vol. 10702, Ground-based and Airborne Instrumentation for Astronomy VII. SPIE, Bellingham, p. 107027V

Scott N. J., Millan-Gabert R., Lhomé E., Ten Brummelarr T. A., Coudé Du Foresto V., Sturmann J., Sturmann L., 2013, J. Astron. Instrum., 02, 1340005

Sliski D. H., Blake C. H., Eastman J. D., Halverson S., 2023, Astron. Nachr., 344, 5

Spaleniak I., Jovanovic N., Gross S., Ireland M. J., Lawrence J. S., Withford M. J., 2013, Opt. Express, 21, 27197

Vigan A. et al., 2024, A&A, 682, A16

Virtanen P. et al., 2020, Nat. Methods, 17, 261

This paper has been typeset from a TEX/LATEX file prepared by the author.